






Cite this: *J. Mater. Chem. C*, 2022, 10, 5608

## Tailoring the anion stoichiometry and oxidation kinetics of vanadium (oxy)nitride by the control of ammonolysis conditions†

Laura I. V. Holz,  <sup>abc</sup> Vanessa C. D. Graça, <sup>a</sup> Francisco J. A. Loureiro,  <sup>a</sup> Sergey M. Mikhalev, <sup>a</sup> Diogo Mendes, <sup>c</sup> Adélio Mendes  <sup>b</sup> and Duncan P. Fagg <sup>a</sup>

Transition metal (oxy)nitrides are attractive materials due to their notable catalytic and electronic properties. Vanadium (oxy)nitrides, in particular, have generated high interest due to their wide applicability in heterogeneous catalysis, energy-related research (e.g., supercapacitors), and superconductors. One of the most promising ways to synthesize these materials is by ammonolysis. However, thermodynamic calculations predict that the chemical potentials of both the nitrogen and hydrogen precursors are dependent on the synthesis temperature, potentially influencing the N/O ratio of the formed (oxy)nitride. The current work, therefore, clarifies the effect of ammonolysis temperature on the (oxy)nitride composition and resultant physical properties. A series of vanadium (oxy)nitrides are formed by reacting  $V_2O_5$  with gaseous ammonia in the temperature range 600–1000 °C. The synthesized materials are characterized by X-ray diffraction (XRD), scanning electron microscopy (SEM), thermogravimetry (TGA), and X-ray photoelectron spectroscopy (XPS). The unit cell volume of the crystal is shown to increase with ammonolysis temperature, being concomitant with increased nitrogen incorporation. Kinetic analysis was performed by isoconversional and model-based methods, showing that the amount of incorporated nitrogen has a strong impact on materials stability, beneficially increasing the resistance towards oxidation. The work demonstrates that it is possible to compositionally tune the anionic sublattice of vanadium (oxy)nitride by controlling the ammonolysis temperature, where this method can be used as a tool to tailor resultant properties towards potential applications.

Received 8th February 2022,  
Accepted 8th March 2022

DOI: 10.1039/d2tc00545j

rsc.li/materials-c

## 1. Introduction

Transition metal (oxy)nitrides (TMNs), commonly known as interstitial alloys, have attracted interest due to their exceptional electrical and thermal conductivity, high hardness, and high melting points.<sup>1–6</sup> Due to this unique combination of properties, they are a topic of growing interest in a wide range of applications, such as energy-related research (i.e., electrochemical energy storage devices),<sup>7</sup> superconductors,<sup>8</sup> and also heterogeneous catalysis.<sup>9</sup> For example, TMNs have been considered excellent candidates for the next generation of supercapacitors (SCs), where, among the TMNs, vanadium nitride (VN)

has been extensively studied due to its notable mechanical strength, low cost, good chemical stability and impressive specific capacitance ( $1340 \text{ F g}^{-1}$  at  $2 \text{ mV s}^{-1}$ ).<sup>6</sup> TMNs also have been studied as potential superconducting materials<sup>10,11</sup> with considerable interest for electronic applications, such as integrated circuits and electromagnets.<sup>12</sup> In particular, VN offers a relatively high transition temperature that is experimentally shown to range from 2 to 9 K.<sup>10</sup>

A further growing application of TMNs is that of heterogeneous catalysis, in the search for new reaction systems with increased selectivity. In this respect, the majority of industrially relevant chemical processes still rely on catalysts based on noble metals for the synthesis of added-value chemical products.<sup>13</sup> Such systems have several known disadvantages, such as high cost, low availability, susceptibility to poisoning and can also have detrimental effects on the environment.<sup>14</sup> As an alternative, monometallic nitrides have shown to be very promising for the substitution of noble metals in a variety of catalytic processes, including Fischer–Tropsch synthesis,<sup>15</sup> ammonia synthesis<sup>16,17</sup> and other hydrogenation reactions,<sup>18</sup> exhibiting exceptional activity and selectivity for these reactions,

<sup>a</sup> Centre for Mechanical Technology and Automation, Mechanical Engineering Department, University of Aveiro, Aveiro, 3810-193, Portugal.  
E-mail: lauraholz@ua.pt

<sup>b</sup> LEPABE - Faculdade de Engenharia, Universidade do Porto, rua Dr Roberto Frias, 4200-465 Porto, Portugal

<sup>c</sup> Bondalti Chemicals, S.A., Quinta da Indústria, Rua do Amónio Português no. 10, Beduído e Veiros, Estarreja 3860-680, Portugal

† Electronic supplementary information (ESI) available. See DOI: 10.1039/d2tc00545j

**Table 1** Properties of oxygen and nitrogen. Adapted from<sup>5</sup>

	N	O
Anion charge	−3	−2
Electronegativity	3.0	3.4
Atomic polarizability/Å <sup>3</sup>	1.10	0.80
Electronic affinity (A → A <sup>z−</sup> kJ <sup>−1</sup> mol <sup>−1</sup> )	1736	601
Ionic radii/Å (for CN=IV)	1.46	1.38
Coordination number (CN)	II–VIII	II–VIII

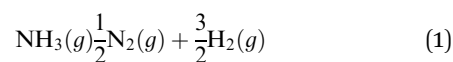
while also offering greater abundance and lower cost. In particular, VN has been shown to be a very promising candidate for ammonia decomposition, as an alternative to Pt group metals.<sup>19,20</sup>

Generally, this family of nitride materials exhibits face-centered cubic structures (*fcc*), where smaller nitrogen atoms occupy the interstitial positions of the host lattice.<sup>10,21</sup> One key feature of these materials concerns their ability to simultaneously incorporate both oxygen and nitrogen into the anionic sublattice, potentially allowing these materials to benefit from the combined properties of both oxides and nitrides. Nonetheless, current literature targeting modifications to the anionic lattice is still in its infancy, with most works alternatively concentrating on substitutions on the cation lattice. Thus, manipulation of the (oxy)nitride materials by adjusting the ratio of N/O atoms in their anionic lattice, as in the current work, can expand existing knowledge of these materials to potentially provide a new route for their properties tailoring.<sup>22,23</sup>

The substitution of oxygen for nitrogen in these materials is relatively straightforward, due to their similar ionic radii, leading to large solid solution ranges of N/O ratio. Furthermore, the differing valencies, electronegativities, and polarizabilities of N and O anions (Table 1) can have great impact upon the resultant properties of the oxynitrides.<sup>5,22</sup> For example, this feature has been shown to be beneficial for the application of (oxy)nitrides in a variety of important catalytic processes.<sup>24</sup> Here, the electronic structure of these materials can be greatly influenced by the nitrogen 2p orbitals, which possess higher energy when compared to those of oxygen.

Thus, the introduction of nitrogen into the oxygen sublattice can potentially manipulate resultant properties to benefit different applications.

Previous studies suggested several routes for the synthesis of polycrystalline oxynitrides, such as the use of urea as a nitrogen source,<sup>10,25</sup> microwave synthesis,<sup>26–28</sup> hydrothermal synthesis,<sup>29</sup> high-temperature plasma routes,<sup>30</sup> mechanochemical synthesis under pressurized atmosphere,<sup>31</sup> the direct reaction of metal vanadium and nitrogen, and the direct ammonolysis of oxide precursors, aerogels, sulfides and metal amides.<sup>32–35</sup> In the current study, we focus on VON materials prepared by the ammonolysis route, involving the nitridation of vanadium pentoxide (V<sub>2</sub>O<sub>5</sub>) by its reaction with gaseous ammonia (NH<sub>3</sub>) at elevated temperature. The calculated Gibbs free energy ( $\Delta G_R$ ) of the reduction-nitridation process of V<sub>2</sub>O<sub>5</sub> to VN conversion is plotted as a function of temperature in Fig. 1a. This plot highlights that the ammonolysis of V<sub>2</sub>O<sub>5</sub> (solid blue line in Fig. 1a) is thermodynamically possible over a wide temperature range, becoming increasingly energetically favorable with increasing temperature. At the same time, ammonia decomposition is also thermodynamically favorable for  $T > 185$  °C, decomposing into N<sub>2</sub> and H<sub>2</sub> (Fig. 1a and b):



$$\Delta G^\circ = \frac{1}{2}(3\Delta\mu_{\text{H}_2} + \Delta\mu_{\text{N}_2}) = RT(1.5 \ln p_{\text{H}_2} + 0.5 \ln p_{\text{N}_2}) \quad (2)$$

where  $p_{\text{H}_2}$  and  $p_{\text{N}_2}$  correspond to the partial pressures of H<sub>2</sub> and N<sub>2</sub>, respectively. Nevertheless, one should mention that the kinetic limit of ammonia decomposition (vertical blue dashed line) is well above its predicted stability limit.<sup>34</sup> In fact, it is well known that, for an efficient thermal activation, a minimum temperature of ~550 °C is necessary for ammonia dissociation (N–H bond strength is 3.9 eV).<sup>34</sup> For the ammonolysis reaction, this is of vital importance since, above this temperature, ammonia can be rapidly decomposed at ambient pressure. In such conditions, the chemical potentials of both hydrogen ( $\Delta\mu_{\text{H}_2}$ ) and nitrogen

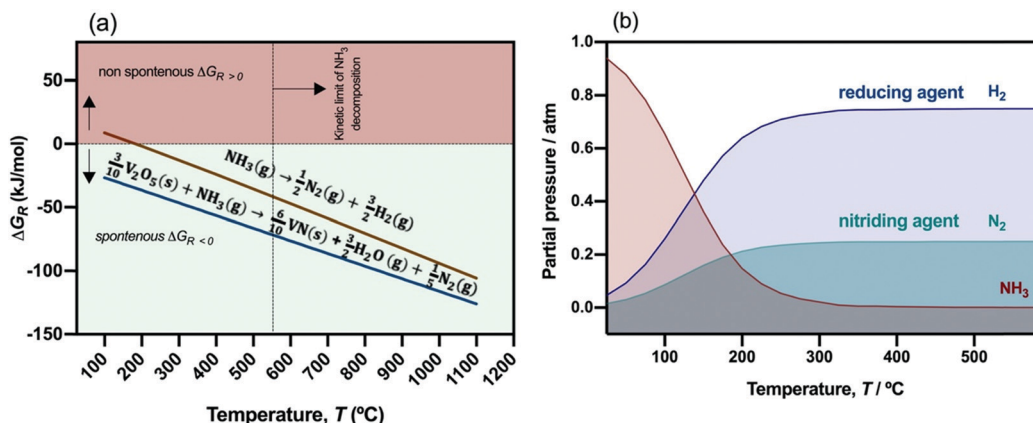
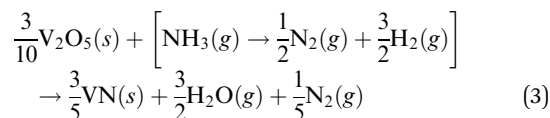


**Fig. 1** (a) Gibbs free energy ( $\Delta G_R$ , kJ mol<sup>−1</sup>) as a function of temperature ( $T$ , °C) for the ammonolysis of V<sub>2</sub>O<sub>5</sub> precursor; (b) temperature dependence of equilibrium partial pressures of NH<sub>3</sub>, N<sub>2</sub>, and H<sub>2</sub> at 1 atm total pressure (thermodynamic data collected from Factsage software<sup>36</sup>).

( $\Delta\mu_{\text{N}_2}$ ) are very high; a situation that is equivalent to the use of high-pressure  $\text{N}_2$  or  $\text{H}_2$  gases, typically required at much lower temperatures, for the synthesis shown below:<sup>34</sup>



The high reactivity of the gas species ( $\text{N}_2$  and  $\text{H}_2$ ) is mandatory during the ammonolysis of  $\text{V}_2\text{O}_5$  (eqn (3)). During this reaction, oxygen anions at the oxide surface exchange with adsorbed nitrogen atoms to give nitride anions, with the oxygen being removed into the gas phase where it immediately reacts with high concentrations of surface hydrogen to produce water vapor (solid blue line shown in Fig. 1a). Therefore, one should note that control of the ammonolysis temperature is a critical feature to be able to regulate the reaction pathway to obtain selected vanadium oxynitride phases. In this respect, note that the resultant crystal chemistry is strongly affected by the thermal activation of ammonia, which is controllable by the synthesis temperature and that important changes in the N/O ratio of the (oxy)nitride phases can also be generated with extensive impact on the resultant physical and chemical properties of the (oxy)nitride.

Hence, this article clarifies the effect of ammonolysis temperature on the phase composition and properties of vanadium (oxy)nitride solid-solutions. The effect of ammonolysis temperature and time is evaluated in the temperature range 600 – 1000 °C, with the assessment of its impact on crystal chemistry (crystal size, lattice strain, lattice expansion) and on the stability of the (oxy)nitride towards oxidation, developing a controllable method to tune the resultant materials.

## 2. Experimental procedure

### 2.1. Materials synthesis by ammonolysis route

The ammonolysis route was employed to produce a series of vanadium (oxy)nitrides by thermal nitridation of a  $\text{V}_2\text{O}_5$  powder (Sigma-Aldrich, >99.6%), using flowing ammonia gas ( $\text{NH}_3$ ). For this purpose, 0.3 g of  $\text{V}_2\text{O}_5$  precursor was placed in an alumina crucible, which was then inserted inside a tubular furnace. The precursor powder was heated at different temperatures (600, 700, 800, 900, and 1000 °C) under flowing  $\text{NH}_3$  (50 mL min<sup>-1</sup>) and heating/cooling rates 5 °C min<sup>-1</sup>. Different ammonolysis dwell times (1, 4, 8 and 12 h) were studied at the lower temperature tested (*i.e.*, 600 °C) to assess the equilibrium conditions. After cooling, the calcinated powders were subjected to a passivation procedure by switching the gas to  $\text{N}_2$  at room temperature for 30 minutes.

### 2.2. Microstructural characterization

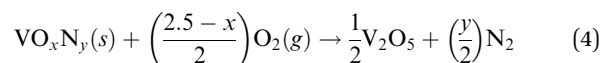
The powder morphology was observed by Scanning Electron Microscopy (SEM), *Hitachi TM4000 plus*. The analysis was done on both the precursor ( $\text{V}_2\text{O}_5$ ) and the calcined powders that were placed on a carbon tape. The microscope was operated

using an applied voltage of 10–15 kV and a Backscattered Electron (BSE) detector.

### 2.3. Nitrogen and oxygen content

The nitrogen content of the produced materials was calculated by an elemental chemical analyzer (LECO, CHNS-932).

The oxygen content was determined by thermogravimetric experiments (*NETZSCH TG 209*) as reported elsewhere,<sup>37</sup> by measuring the mass variation of the conversion of the VON samples transformed into orthorhombic  $\text{V}_2\text{O}_5$  by heating under oxygen ( $\text{O}_2$ ) atmosphere at 600 °C:



The powdered samples were heated at 3 °C min<sup>-1</sup>, using a dwell time of 10 hours, and a cooling rate of 5 °C min<sup>-1</sup>. For these measurements, the final products were structurally characterized by X-ray diffraction (XRD) to ensure that the starting and the final states are pure and well-defined phases.<sup>37</sup>

### 2.4. Structural characterization

The structural characterization of VON materials was performed by XRD using a *Rigaku SmartLabSe* diffractometer (Cu K $\alpha$  radiation – 1.5406 Å, 40 kV, 30 mA). The XRD patterns were collected in the range 20° < 2 $\theta$  < 100°, with a scan speed of 3° min<sup>-1</sup>. The lattice parameters of the synthesized VON powders were determined using the *Rietveld* refinement method to the XRD data in the *SmartlabStudio* software. In the present study, a pseudo-Voigt peak profile function was used for the profile fitting and the background was fitted with the B-spline function.

### 2.5. X-Ray photoelectron spectroscopy (XPS)

XPS spectra were acquired in an Ultra High Vacuum (UHV) system with a base pressure of 2 × 10<sup>-10</sup> mbar. The system was equipped with a hemispherical electron energy analyzer (SPECS *Phoibos 150*), a delay-line detector and a monochromatic Al-K $\alpha$  (1486.74 eV) X-ray source. High resolution spectra were recorded at normal emission take-off angle and with a pass-energy of 20 eV, which provides an overall instrumental peak broadening of 0.5 eV. The XPS spectra were fitted using the *XPSPeak 4.1* software, where the number of peaks, the full width at half maximum (FWHM), positions and shapes (% of Lorentzian and Gaussian functions used) were optimized to obtain the best fit.

### 2.6. Kinetic model by thermogravimetry

In this work, the kinetic study was developed by thermogravimetric experiments (*NETZSCH TG 209*) by measuring the conversion of the vanadium (oxy)nitride samples transformed into orthorhombic  $\text{V}_2\text{O}_5$  by heating under oxygen ( $\text{O}_2$ ) atmosphere to a maximum temperature of 600 °C under different heating rates (0.5, 1, 3, and 5 °C min<sup>-1</sup>). More information concerning

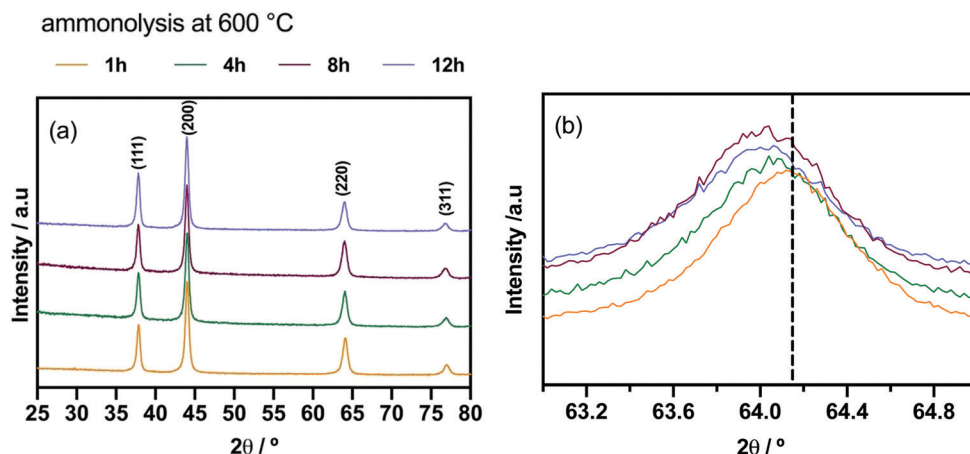


Fig. 2 (a) XRD patterns of VON material synthesized at 600 °C at different dwell times of 1, 4, 8 and 12 h (b) XRD patterns expanded in the high  $2\theta$  range, emphasizing the shift in peak position.

the kinetic methods applied in this work can be found in the ESI.†

### 3. Results and discussion

#### 3.1. Structural characterization

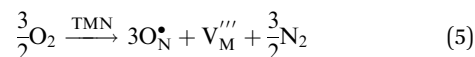
Fig. 2 shows the XRD patterns of the VON powder synthesized at the lowest preparation temperature (600 °C) for different dwell times. The observed diffraction peaks can all be indexed with a cubic structure, space group  $Fm\bar{3}m$  (ICDD card 00-035-0768), supporting the successful formation of phase pure samples. This crystallographic structure is characteristic of the vanadium (oxy)nitride rock-salt type structure, in which metal atoms are in a *fcc* arrangement with non-metals occupying the interstitial positions.<sup>38</sup> Fig. 3 highlights an increase in calculated lattice parameter with increasing synthesis time of up to 8 h, which can be related with an associated increase in N-content, and respective decrease in O-content, of the (oxy)-nitride Fig. 3, which were calculated by a combination of TGA and elemental analysis (see ESI† Fig. S1 and Table S1). Both the

lattice parameter and anion contents are observed to become constant after 8 h of synthesis time, suggesting that compositional equilibrium was reached at this synthesis temperature. To subsequently study the impact of ammonolysis temperature on the crystal chemistry, a fixed dwell time of 12 h was, therefore, selected for the remaining experiments, to ensure that equilibrium conditions were obtained for synthesis temperatures of 600 °C and above.

Fig. 4 shows the XRD patterns of VON powder prepared at different temperatures with a dwell time of 12 h. It is interesting to note that there are significant deviations in the peak positions towards lower  $2\theta$  angles for higher calcination temperatures, as highlighted in Fig. 4b. This observation can be attributed to an increase in lattice parameter and respective increase in unit cell volume as the ammonolysis temperature rises, Table 2.

The defect chemistry adopted for nitrogen and oxygen incorporation in vanadium (oxy)nitride materials remains a point of open discussion in the literature, with no definitive knowledge being currently provided with regards to the most likely point defects for any specific nitride.<sup>17,39</sup> Nonetheless, a recent work by Balasubramanian *et al.*,<sup>40</sup> using first-principle calculations, suggests that the formation of metal vacancies may be thermodynamically favorable for this type of group (V), rock salt structure, nitrides.

The defect chemistry of the VON compound was, therefore, assigned to the substitution of nitrogen by oxygen in the anionic lattice, followed by the creation of cation vacancies, as illustrated by equation (Kröger-Vink notation):



where TMN denotes a transition metal nitride,  $\text{O}_\text{N}^\bullet$  is a positive defect due to oxygen ( $\text{O}^{2-}$ ) occupying a regular site of nitrogen ( $\text{N}^{3-}$ ), and  $\text{V}_\text{M}'''$  denotes a net negatively charged vanadium vacancy. To maintain lattice electroneutrality, the defect mechanism, therefore, suggests no change in the vanadium oxidation

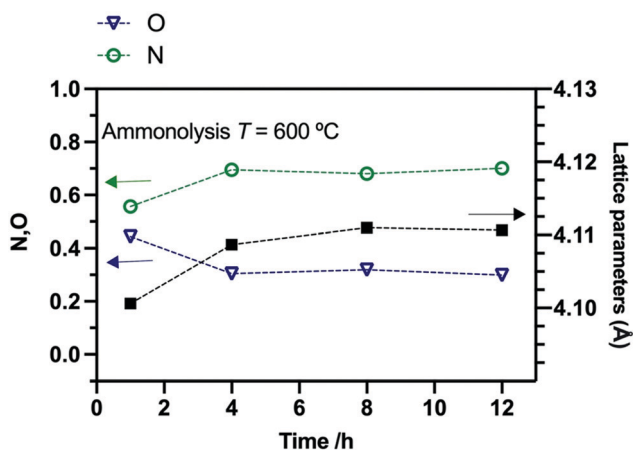


Fig. 3 N/O content (left) and lattice parameters (right) as a function of ammonolysis time.



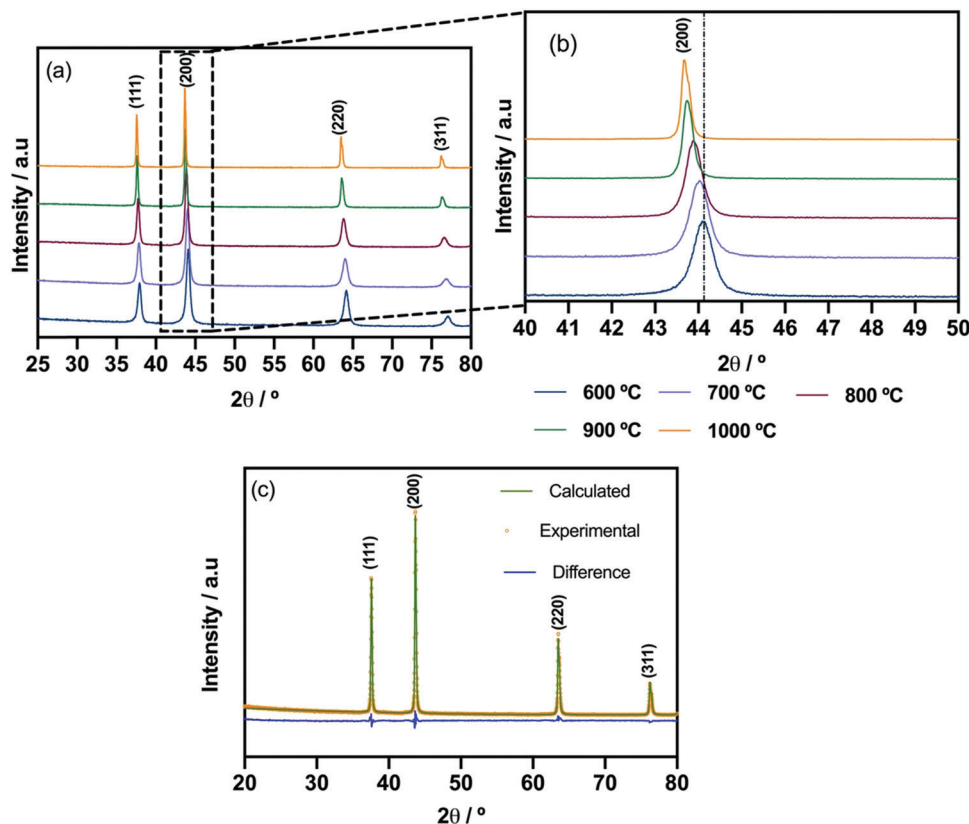


Fig. 4 (a) XRD pattern of VON compositions prepared at different temperatures with a dwell time of 12 h; (b) inset showing the peak shift; (c) XRD pattern resulted from the *Rietveld* refinement.

Table 2 Structural parameters obtained by refinement using the *Rietveld* method for different compositions

Temperature (°C)	600	700	800	900	1000 (12 h)
Space group	<i>Fm</i> $\bar{3}$ <i>m</i> (cubic symmetry)				
Lattice parameters, $a = b = c$ (Å)	4.1106(4)	4.1278(3)	4.1367(3)	4.1377(2)	4.1378(9)
$\alpha = \beta = \gamma$ (°)	90				
$V_m$ (Å <sup>3</sup> )	69.458(9)	70.334(2)	70.789(9)	70.844(3)	70.845(9)
$R_{wp}$ (%)	8.75	6.39	8.03	7.69	3.46
$S$	1.94465	1.7929	1.7918	1.0670	1.2009

$V_m$ , unit cell volume;  $R_{wp}$  and  $S$ , statistical factors of the goodness of fit of *Rietveld* adjustment; numbers in parentheses are standard deviations.

state ( $3^+$ ) but, instead, outlines a charge compensation mechanism based on the creation of cationic vacancies ( $V_M'''$ ).

The compositions of the VON powders prepared at different temperatures are indicated in Table 3, arising from N and O contents and cation/anion ratios obtained experimentally by

Table 3 Measured normalized composition ( $N + O = 1$ ) and corresponding V oxidation state

Ammonolysis temperature/°C	Normalized composition	V oxidation state
600	$V_{0.86}O_{0.30}N_{0.70}$	3.14
700	$V_{0.89}O_{0.22}N_{0.78}$	3.12
800	$V_{0.93}O_{0.10}N_{0.90}$	3.12
900	$V_{0.94}O_{0.08}N_{0.92}$	3.11
1000	$V_{0.98}O_{0.06}N_{0.94}$	3.00

combination of TGA and elemental analysis. Fig. 5 exhibits the obtained TGA curves for different ammonolysis temperatures.

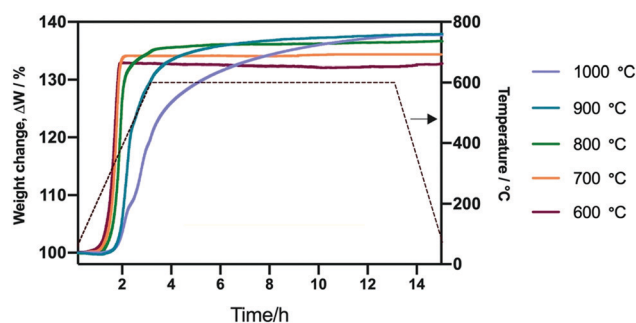


Fig. 5 TGA of selected materials produced at different temperatures for a fixed dwell time of 12 hours in  $O_2$  at 600 °C.

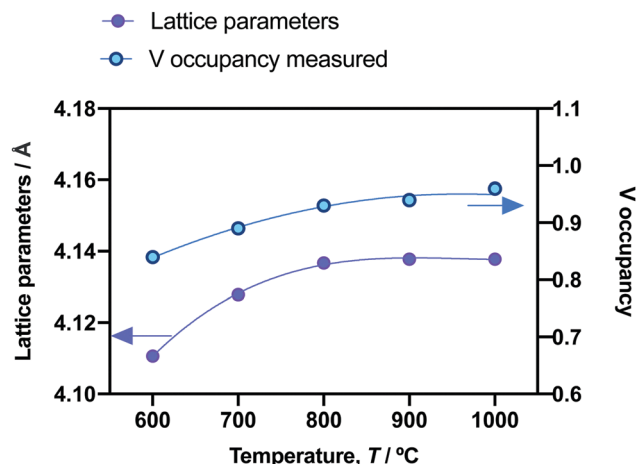


Fig. 6 Lattice parameters and V occupancy measured experimentally as a function of ammonolysis temperature.

The weight gain of the compounds is shown to be greater for samples of a higher synthesis temperature, implying that higher temperatures are favourable to obtain (oxy)nitrides with lower oxygen content and, consequently, higher nitrogen content.

Therefore, the results highlight a significant increase in the N-content with the ammonolysis temperature, at the detriment of the O-content. Fig. 6 plots the lattice parameters of these samples, as a function of ammonolysis temperature, against the V occupancy, which was calculated upon normalizing the experimental compositions to a total anion occupancy of unity. As can be seen, the increase in unit cell parameter with ammonolysis temperature can be correlated with a decrease in the number of vanadium vacancies, as the samples accommodate increasingly more nitrogen with increasing ammonolysis temperature, Table 3. The expected vanadium oxidation state arising from the measured compositions presents values close to 3+, Table 3, an observation that reinforces the defect chemical mechanism indicated in Eqn (5).

### 3.2. Microstructural characterization

Scanning Electron Microscopy (SEM) was used to evaluate the effect of ammonolysis temperature on the powder morphology. The SEM images depicted in Fig. 7 show that the powders exhibit crystalline fragments with columnar crystal forms. From the figure, it can also be concluded that the ammonolysis temperature does not significantly impact the powder morphology, since the overall particle size and shape are independent on ammonolysis temperature, being similar to that of the  $V_2O_5$  precursor (Fig. 7a).

### 3.3. XPS measurements

The surface chemical composition and bonding configuration of the samples were also investigated. The XPS technique is very useful to study the surface composition of materials (to depths of 2–4 nm), allowing to estimate the nature of the vanadium cation and the N and O species, quantitatively.<sup>33</sup> The XPS spectrum (Fig. 8a) of the sample prepared at 1000 °C reveals that the material is composed principally of V, N and O, consistent with the XRD studies previously shown in Fig. 2, and with some C from air contamination.

Fig. 8b and c show the high-resolution XPS spectra of O 1s V 2p and N 1s, respectively. To deconvolute the V 2p region, three components with different Binding Energy (BE) were added, according to the literature.<sup>33,41</sup>

As shown in Fig. 8c, the component centered at 513.4 eV and 520.9 eV can be attributed to VN, while peaks at 514.5, 522.7, 516.5 and 524.3 eV can be ascribed to the  $V^{3+}$  and  $V^{5+}$  oxidation states present in vanadium oxides ( $V_2O_3$  and  $V_2O_5$ , respectively).<sup>42</sup> The presence of VN can be observed in the V 2p spectra, while oxidation at the surface can be deduced, from the presence of vanadium species with higher oxidation state, such as  $V_2O_5$ , in accordance with the analysis of the high-resolution O 1s XPS spectrum in Fig. 8b. It should be noted that the dominant presence of the  $V^{3+}$  oxidation state corresponds well with the

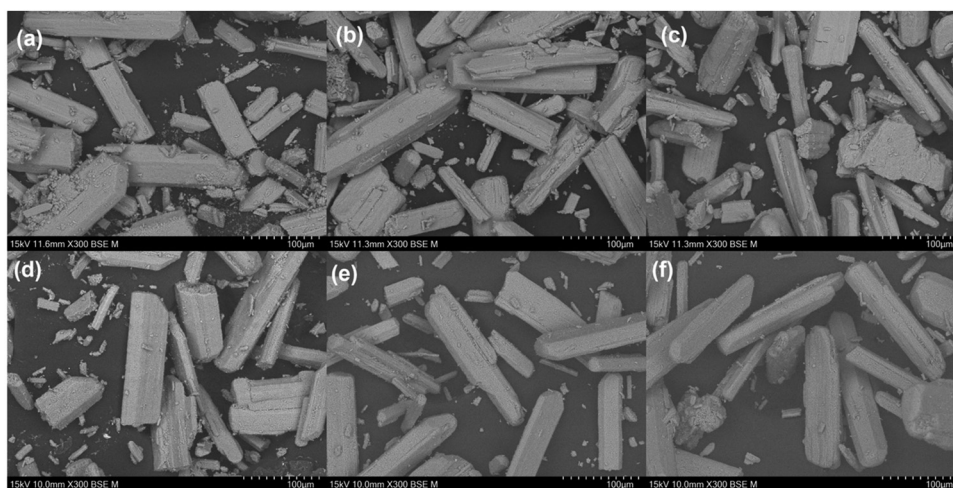


Fig. 7 SEM micrographs of (a)  $V_2O_5$  precursor and VON powders synthesized by ammonolysis route during 12 h at (b) 600 °C, (c) 700 °C, (d) 800 °C, (e) 900 °C and (f) 1000 °C.

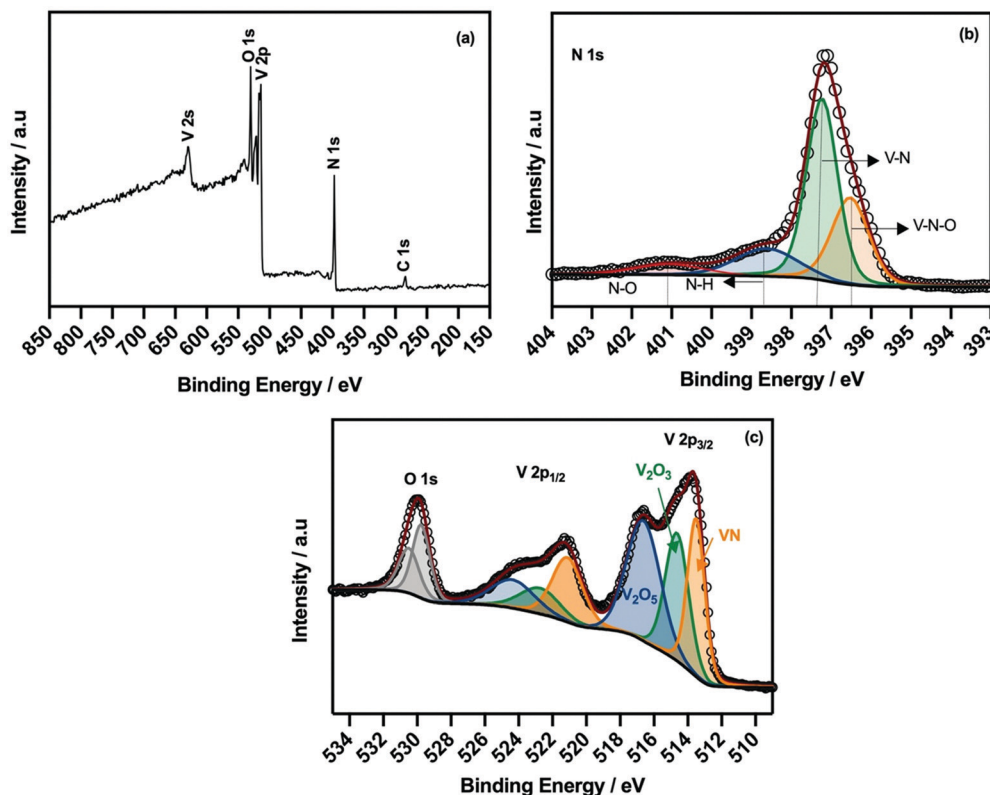


Fig. 8 (a) XPS overview survey of VON (thermally treated at 1000 °C) and high-resolution XPS spectrum of: (b) N 1s region and (c) O 1s and V 2p regions.

defect chemical mechanism of Eqn (5) and the experimentally determined compositions in Table 3.

The O 1s region (Fig. 8c) was fitted with two *Gaussian-Lorentzian* components, where the main component is centered at 529.7 eV, which is typical for oxygen bound to a metal (in this case, V–O).<sup>33</sup> The second small peak at 530.3 eV can be ascribed to O–H groups chemisorbed at the surface.<sup>33,43</sup> The N 1s region was deconvoluted into four components corresponding to V–N, V–N–O, N–H and N–O,<sup>42–44</sup> where the presence of N–H groups is a commonly reported observation, due to the use of NH<sub>3</sub> during synthesis.<sup>37</sup>

### 3.4 Kinetic model

The impact of the (oxy)nitride composition on the material stability was studied by TGA/DSC performed in a flowing oxygen atmosphere. For this purpose, three different compositions were selected: V<sub>0.86</sub>O<sub>0.30</sub>N<sub>0.70</sub>, V<sub>0.93</sub>O<sub>0.10</sub>N<sub>0.90</sub> and V<sub>0.98</sub>O<sub>0.06</sub>N<sub>0.94</sub>. Fig. 9 depicts the TGA/DSC plots, measured at a fixed heating rate of 5 °C min<sup>−1</sup>, revealing that both the onset of the weight gain and the exothermic peak associated with the oxidation process shift towards higher temperatures for (oxy)nitride compositions containing higher N/O ratios. Furthermore, the TGA curve for the low N/O content sample shows a plateau behavior at higher temperatures, corresponding to complete oxidation, while such plateau behavior is not reached for higher N/O ratios. All samples show V<sub>2</sub>O<sub>5</sub> as the final oxidation product upon examination by XRD (results not shown). This oxidation

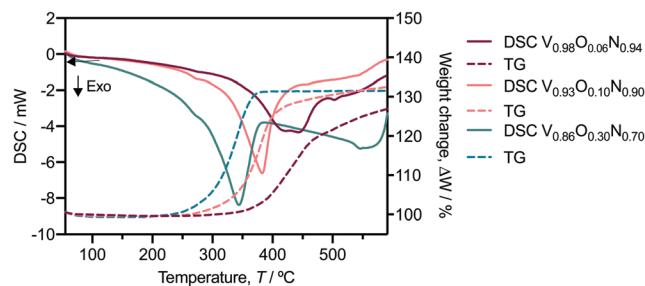


Fig. 9 DSC (solid lines, left side) and weight change (dashed line, right side) as a function of temperature for the different compositions with a heating rate of 5 °C min<sup>−1</sup>.

behavior is now studied in greater depth to extract additional mechanistic information.

### 3.5 Model-free methods

The model-free isoconversion methods allow to estimate the activation energy as a function of the conversion, without previous assumption of the reaction model. This approach can facilitate the detection of multi-step kinetics by the observation of non-linear activation energy dependence as a function of conversion degree. The kinetic parameters obtained by FWO and KAS plots, were determined for the selected compositions (Fig. S2, ESI<sup>†</sup>), providing the activation energy and pre-exponential factors from subsequent linear regression.

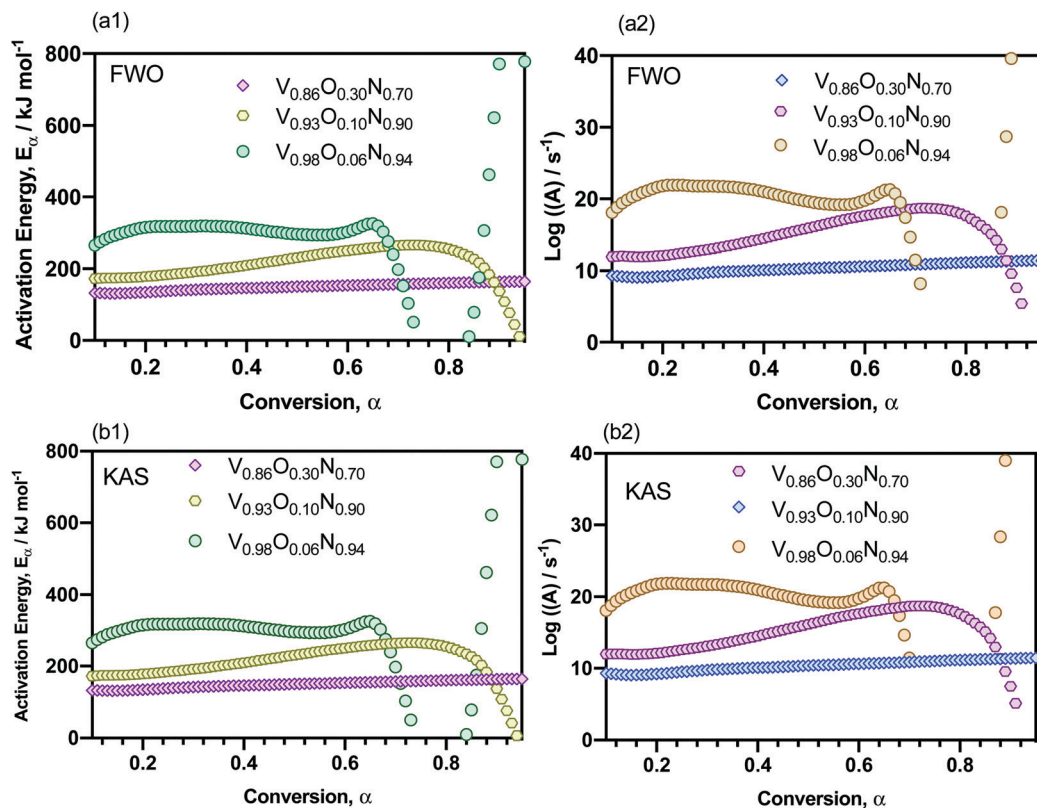


Fig. 10 Activation energy and pre exponential factor of (a1,a2) FWO and (b1,b2) KAS plots for  $V_{0.86}O_{0.30}N_{0.70}$ ,  $V_{0.93}O_{0.10}N_{0.90}$  and  $V_{0.98}O_{0.06}N_{0.94}$  samples, respectively.

In the case of  $V_{0.86}O_{0.30}N_{0.70}$  sample, the linear regression of KAS and FWO plots could be performed for conversions,  $0.1 < \alpha < 0.98$ . However, in the case of the  $V_{0.93}O_{0.10}N_{0.90}$  sample, the model-free analysis could only be performed from  $0.1 < \alpha < 0.85$ , while for the  $V_{0.98}O_{0.06}N_{0.94}$  composition the suitable range of conversion was further limited to  $0.1 < \alpha < 0.65$ . These variations highlight that the last two compositions are likely to exhibit multi-step kinetic behavior, in contrast to the  $V_{0.86}O_{0.30}N_{0.70}$  sample. In agreement, the apparent activation energy derived from the FWO and KAS methods was shown to be non-uniform for different ranges of conversion for the higher N/O ratio samples, indicating the existence of more complex multi-step oxidation mechanisms (Fig. 10).

### 3.6. Model-based methods

Thus, to deepen the study on the mechanism of oxidation, the TGA data were assigned to potential kinetic functions that could best describe the reaction process for each composition.

In the case of the  $V_{0.86}O_{0.30}N_{0.70}$  sample, a three-dimensional diffusion model ( $D_3$ ) was found to be successful to fit the experimental data, suggesting a single-step reaction (A to B), as depicted in Fig. 11(a1 and a2). In this sense, the model-dependent analysis reveals that the oxidation process may assume three-dimensional diffusion as the rate-determining step and that a single rate-determining step can satisfactorily explain the overall conversion. One may, therefore, envisage this reaction as a particle consisting of VN core with a growing

vanadium oxide ( $V_2O_5$ ) shell, which extends by radial diffusion until the total oxidation of the (oxy)nitride. This single step process is described by an activation energy of  $162.8 \text{ kJ mol}^{-1}$  and pre-exponential factor ( $A$ ) of  $10^{10} \text{ s}^{-1}$ , as shown in Table 4.

As indicated by the model-free analysis, the  $V_{0.93}O_{0.10}N_{0.90}$  and  $V_{0.98}O_{0.06}N_{0.96}$  samples show more complex multi-step kinetic behaviors, consisting of several rate-determining steps. In the case of  $V_{0.93}O_{0.10}N_{0.90}$ , the experimental data was fitted using four-steps of different reaction types, as shown in Fig. 11(b1 and b2). Table 5 shows that the first step (A to B) could be successfully modeled using a  $D_3$  reaction type equation, showing the highest contribution (0.6) to the overall process, with an apparent activation energy of  $178.30 \text{ kJ mol}^{-1}$  and pre-exponential factor of  $10^{11} \text{ s}^{-1}$ . The consecutive B to C step was assigned to a  $F^n$  order reaction type (order of 1.98) with an apparent activation energy of  $346 \text{ kJ mol}^{-1}$  and pre-exponential factor of  $10^{35} \text{ s}^{-1}$ . The C to D step was governed by a  $F^n$  order reaction type (order of 3.90) with an apparent activation energy of  $123.23 \text{ kJ mol}^{-1}$  and pre-exponential factor of  $10^7 \text{ s}^{-1}$ . Finally, the last step D to E was also modeled with a  $F^n$  reaction order type (order of 6.370) with an apparent activation energy of  $194.38 \text{ kJ mol}^{-1}$  and pre-exponential factor of  $10^{13} \text{ s}^{-1}$ . The  $F^n$  order reaction steps are most probably associated with sequential vanadium oxide species, of different oxidation states, being formed during the oxidation process (*i.e.*, VO,  $VO_2$  and  $V_2O_5$ ).<sup>45–47</sup> The statistical values underscore a good agreement with the experimental and calculated data.



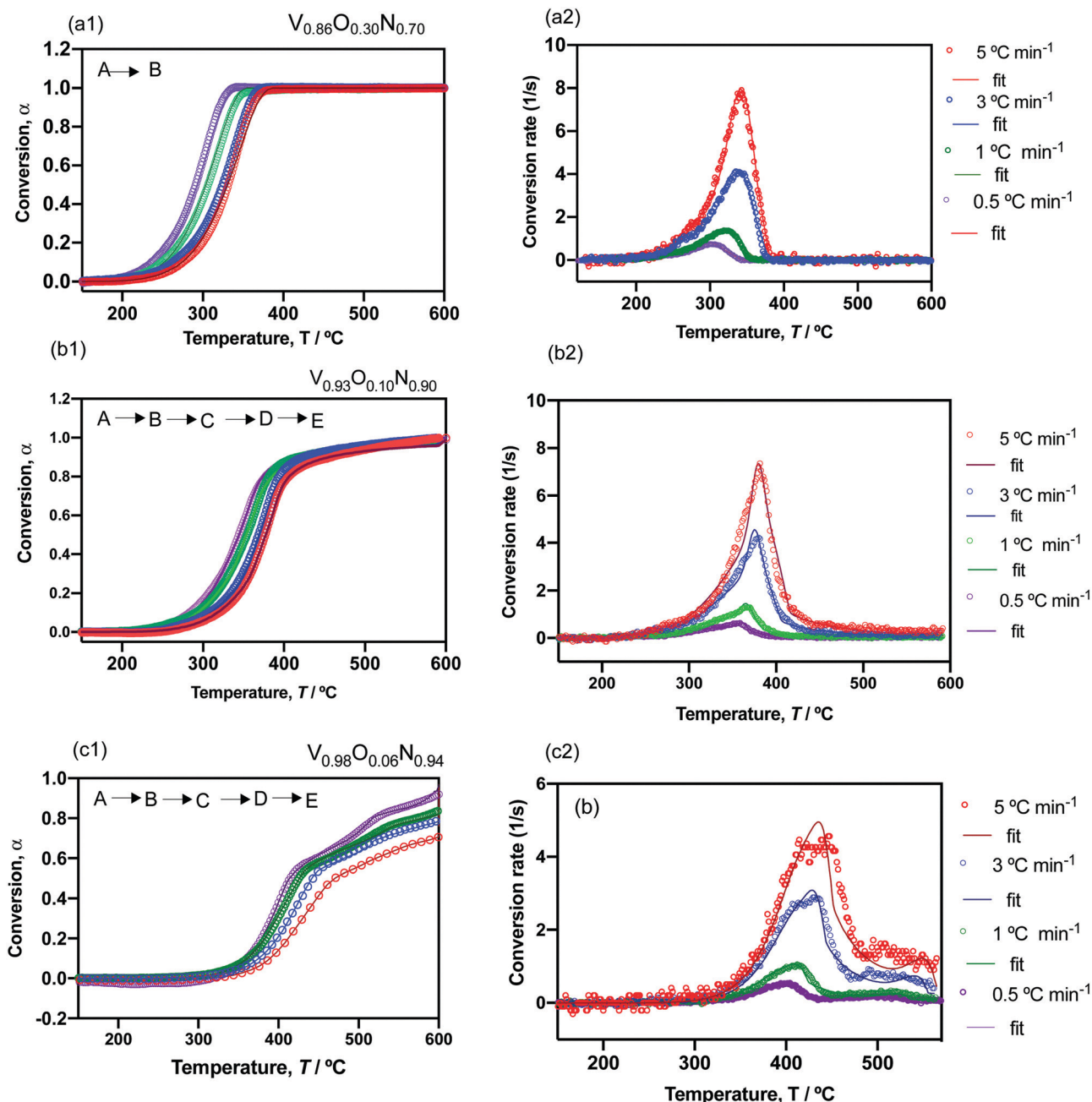


Fig. 11 (a1, b1, c1) Conversion data and fit as a function of temperature and (a2,b2,c2) conversion rate of  $V_{0.86}O_{0.30}N_{0.70}$ ,  $V_{0.93}O_{0.10}N_{0.90}$  and  $V_{0.98}O_{0.06}N_{0.94}$  samples for different heating rates (0.5, 1, 3, and 5 °C min<sup>-1</sup>), respectively.

**Table 4** Kinetic parameters obtained for the sample  $V_{0.86}O_{0.30}N_{0.70}$  model-based analysis. Statistical values such as the sum of deviation squares, mean residual, *F* test and degree of freedom are presented

Step A → B	
Reaction type	Three-dimensional diffusion (D3)
$E_a$ (kJ mol <sup>-1</sup> )	162.882
Log(A (1/s))	10.404
Reaction order	—
Contribution	1
$R^2$	0.99965
Sum of dev squares	197.485
Mean residual	0.247
<i>F</i> test	0.932
Degree of freedom (DF)	1440

**Table 5** Kinetic parameters obtained for  $V_{0.93}O_{0.10}N_{0.90}$  model-based analysis. Statistical values such as the sum of deviation squares, mean residual, *F* test and degree of freedom are presented

Step A → B Step: B → C Step: C → D Step: D → E				
Reaction type	D3	Fn	Fn	Fn
$E_a$ (kJ mol <sup>-1</sup> )	178.31	346.34	123.23	194.38
Log(A)(1/s))	11.04	35.21	7.26	12.66
Reaction order	—	1.98	3.91	6.37
Contribution	0.60	0.18	0.11	0.11
$R^2$	0.99			
Sum of dev squares	105.22			
Mean residual	0.20			
<i>F</i> test	1.00			
DF	1502			

**Table 6** Kinetic parameters obtained for  $V_{0.98}O_{0.06}N_{0.94}$  model-based analysis. Statistical values such as the sum of deviation squares, mean residual, F test and degree of freedom are presented

	Step A → B	Step: B → C	Step: C → D	Step: D → E
Reaction type	D3	F <sup>n</sup>	F <sup>n</sup>	F <sup>n</sup>
$E_a$ (kJ mol <sup>-1</sup> )	279.64	142.38	238.03	190.34
Log (A (1/s))	17.92	6.99	9.96	8.42
Reaction order	—	3.15	0.16	0.14
Contribution	0.42	0.42	0.11	0.05
$R^2$	0.99			
Sum of dev squares	589.79			
Mean residual	0.39			
F test	1.00			
DF	1727			

Finally, for the thermokinetic behavior of  $V_{0.98}O_{0.06}N_{0.94}$  sample (Fig. 11(c1 and c2)), the first step A to B was best fitted

by the D3 model with an apparent energy of 279.60 kJ mol<sup>-1</sup> and pre-exponential factor of 10<sup>18</sup> s<sup>-1</sup> (Table 6). The consecutive step B to C step was assigned to F<sup>n</sup> order reaction type (order of 3.15) with an apparent activation energy of 142.38 kJ mol<sup>-1</sup> and pre-exponential factor of 10<sup>7</sup> s<sup>-1</sup>. The C to D step was governed by to F<sup>n</sup> order reaction type (order of 0.15) with an apparent activation energy of 238.02 kJ mol<sup>-1</sup> and pre-exponential factor of 10<sup>10</sup> s<sup>-1</sup>. Finally, the last step D to E was also modeled with a F<sup>n</sup> reaction order type (order of 0.14) with an apparent activation energy of 190.34 kJ mol<sup>-1</sup> and pre-exponential factor of 10<sup>8</sup> s<sup>-1</sup>. Once again, the F<sup>n</sup> order reaction steps are most probably associated with vanadium oxide species of differing oxidation state formed during the oxidation process (*i.e.*, VO, VO<sub>2</sub> and V<sub>2</sub>O<sub>5</sub>).<sup>45–47</sup>

To support these conclusions, additional experiments were performed to examine the phase contents present at 450 °C in a

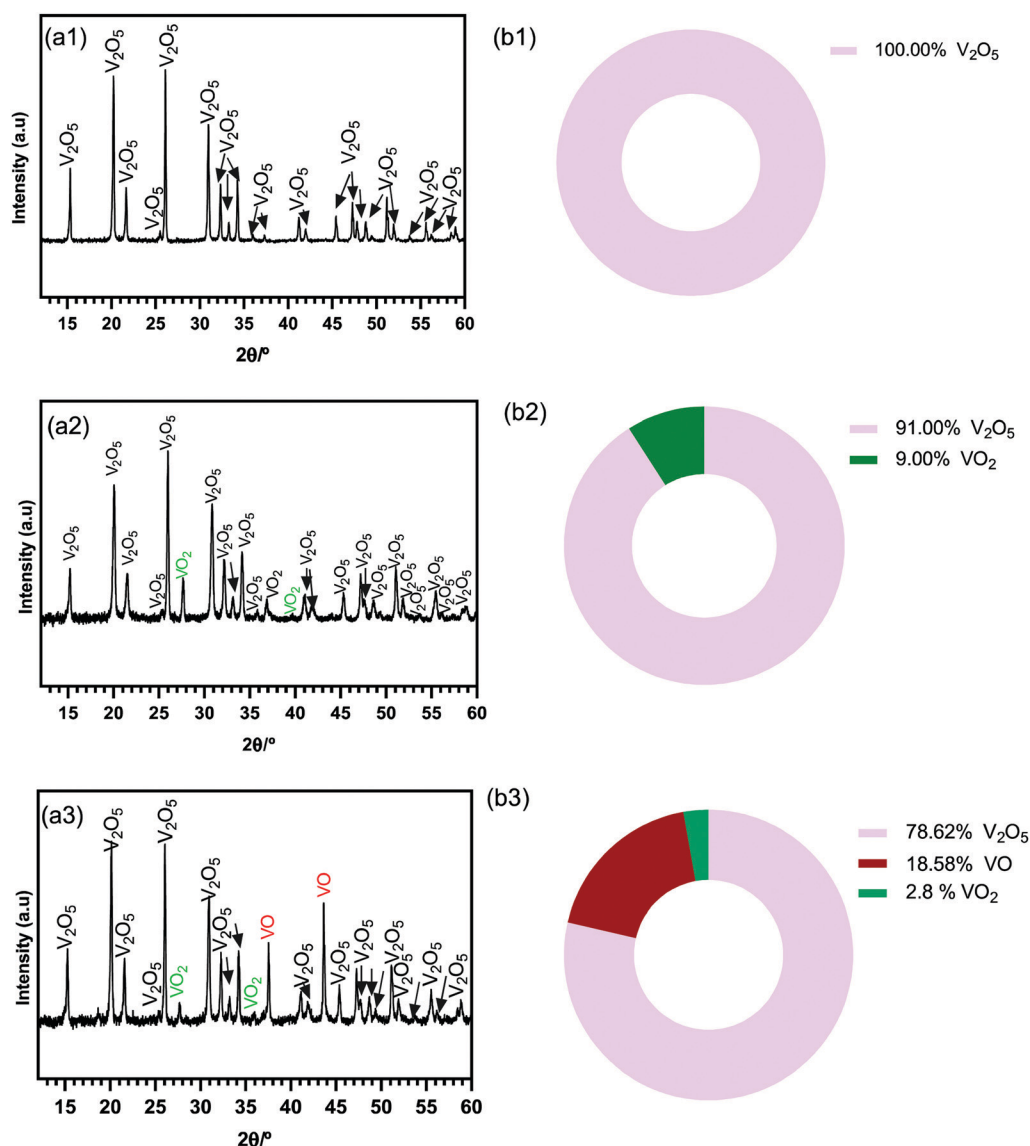


**Fig. 12** (a1–a3) XRD products of  $V_{0.86}O_{0.30}N_{0.70}$ ,  $V_{0.93}O_{0.10}N_{0.90}$  and  $V_{0.98}O_{0.04}N_{0.96}$  samples after quenching at 450 °C in pure oxygen and (b1) (b2) (b3) are the respective phase quantification.

pure oxygen atmosphere for each sample. To do this, the samples were rapidly quenched to room temperature, by removing crucibles from the high-temperature furnace, with subsequent phase analysis by XRD (Fig. 12). In the case of sample  $V_{0.86}O_{0.30}N_{0.70}$ , only the presence of  $V_2O_5$  was observed, in accordance with the aforementioned one step oxidation process of this composition. Conversely, for sample  $V_{0.93}O_{0.10}N_{0.90}$ , 9% of  $VO_2$  was also detected. Finally, for the sample with the highest N content, the XRD analysis shows the presence of 78.62%  $V_2O_5$ , 18.58%  $VO$  and 2.80% of  $VO_2$ . These results, therefore, strongly reinforce the conclusions of the model based kinetic analysis by revealing the presence of vanadium oxides of differing oxidation state (e.g.  $VO$ ,  $VO_2$  and  $V_2O_5$ ). The sequential formation of different vanadium oxidation states concurs with the additional rate-limiting kinetic steps that are observed during the oxidation of these samples of higher N content.

### 3.7. Isothermal prediction

Isothermal predictions were performed to estimate the stability towards oxidation of the samples at different temperatures, as depicted in Fig. 13. The predictions clearly show that the sample with the highest N content ( $V_{0.98}O_{0.06}N_{0.94}$  sample) is significantly more stable towards oxidation than the other compositions. For instance, after 100 minutes in contact with pure oxygen at 350 °C, total conversion of sample  $V_{0.90}N_{0.72}O_{0.28}$  is predicted, while for samples  $V_{0.93}O_{0.10}N_{0.90}$  and  $V_{0.98}O_{0.06}N_{0.94}$  the

conversion is significantly lower, with conversions,  $\alpha = 0.7$  and 0.2, respectively, evidencing the much higher stability of the highest nitrogen-content sample, –  $V_{0.98}O_{0.06}N_{0.94}$ .

## 4. Conclusions

Vanadium (oxy)nitride solid-solutions with a rock-salt structure were successfully produced by the ammonolysis route at synthesis temperatures from 600 to 1000 °C. The ammonolysis temperature was found to have a strong effect on the N/O ratio of the formed (oxy)nitride. This observation can be related to the thermodynamic and kinetic limits for ammonia decomposition that produce the reducing and nitridation effects. Importantly, it was found that the N/O ratio increases with the ammonolysis temperature, as calculated experimentally by combined TGA and elemental analyses. This increase produces a consequent expansion of the unit cell parameters. This phenomenon was successfully explained based on the annihilation of cationic vacancies that are present as charge compensating defects for oxygen accommodation, with the oxidation state of vanadium remaining predominantly that of 3+. Crystalite sizes were shown to increase with ammonolysis temperature while lattice strain decreased, as confirmed by XRD studies.

Importantly, the kinetic analysis shows that an increased ammonolysis temperature and a subsequently higher nitrogen content can be beneficial to improve the stability of the

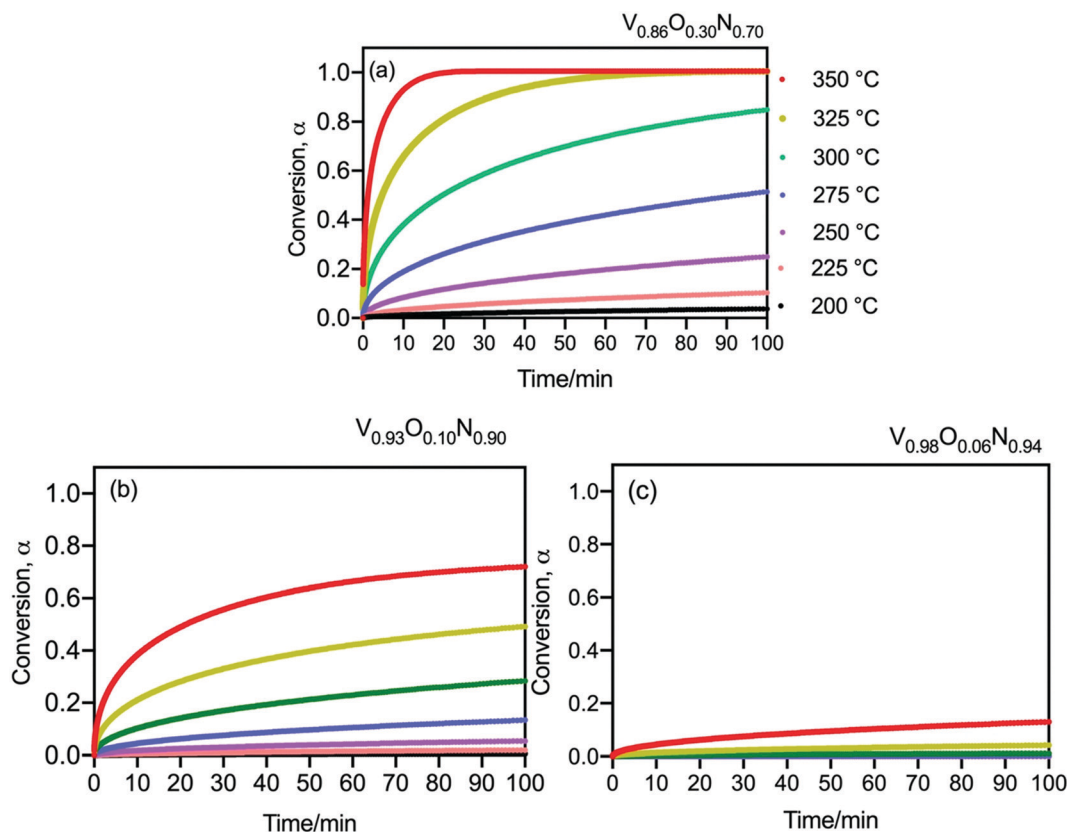


Fig. 13 Isothermal predictions of (a)  $V_{0.86}O_{0.30}N_{0.70}$  (b)  $V_{0.93}O_{0.10}N_{0.90}$  and (c)  $V_{0.98}O_{0.06}N_{0.94}$  samples.

(oxy)nitride towards oxidation. Here, samples with an increased N/O ratio were shown to undergo a more complex oxidation behavior, where the rate determining steps can be best associated with radial oxygen diffusion/ $F^n$  order type reactions, namely the stepwise formation of VO, VO<sub>2</sub> and V<sub>2</sub>O<sub>5</sub> species. This work, therefore, highlights that both the cation/anion ratio and the associated N/O ratio of these materials can be precisely controlled by the ammonolysis temperature, allowing the physical properties of vanadium (oxy)nitride to be tailored towards a wide range of potential applications. As an example, the current work highlights that materials with differing oxygen affinities and oxidation mechanisms can be obtained that can have significant impact on catalytic properties, amongst others.

## Conflicts of interest

The Authors declare that there is no conflict of interest.

## Acknowledgements

Laura I. V. Holz acknowledges Fundação para a Ciência e Tecnologia (FCT) for the PhD grant PD/BDE/142837/2018. Vanessa C. D. Graça acknowledges FCT for the PhD grant SFRH/BD/130218/2017. Francisco J. A. Loureiro is thankful for the Investigator Grant CEECIND/02797/2020. The authors also acknowledge the projects, PTDC/CTM-CTM/2156/2020, PTDC/QUI-ELT/3681/2020, POCI-01-0247-FEDER-039926, POCI-01-0145-FEDER-032241, UIDB/00481/2020 and UIDP/00481/2020 and CENTRO-01-0145-FEDER-022083 – Centro Portugal Regional Operational Programme (Centro2020), under the PORTUGAL 2020 Partnership Agreement, through the European Regional Development Fund (ERDF). The authors acknowledge the Base Funding – UIDB/00511/2020 of the Laboratory for Process Engineering, Environment, Biotechnology and Energy – LEPABE – funded by national funds through the FCT/MCTES (PIDDAC).

## References

- 1 M. Nagai, *Appl. Catal. A Gen.*, 2007, **322**, 178–190.
- 2 P. Liu and J. A. Rodriguez, *Catal. Lett.*, 2003, **91**, 247–252.
- 3 A. M. Alexander and J. S. J. Hargreaves, *Chem. Soc. Rev.*, 2010, **39**, 4388–4401.
- 4 S. T. Oyama, *Catal. Today*, 1992, **15**, 179–200.
- 5 A. Fuertes, *Dalton Trans.*, 2010, **39**, 5949–5964.
- 6 D. Choi, G. E. Blomgren and P. N. Kumta, *Adv. Mater.*, 2006, **18**, 1178–1182.
- 7 J. Shi, B. Jiang, C. Li, F. Yan, D. Wang, C. Yang and J. Wan, *Mater. Chem. Phys.*, 2020, **245**, 122533.
- 8 X. J. Chen, V. V. Struzhkin, Z. Wu, M. Somayazulu, J. Qian, S. Kung, A. N. Christensen, Y. Zhao, R. E. Cohen, H. K. Mao and R. J. Hemley, *Proc. Natl. Acad. Sci. U. S. A.*, 2005, **102**, 3198–3201.
- 9 A. B. Dongil, *Nanomaterials*, 2019, **9**, 1111.
- 10 R. S. Ningthoujam and N. S. Gajbhiye, *Prog. Mater. Sci.*, 2015, **70**, 50–154.
- 11 M. Sahnoun, J. C. Parlebas, M. Driz and C. Daul, *Phys. B Condens. Matter*, 2010, **405**, 3822–3825.
- 12 E. Mohimi, Z. V. Zhang, J. L. Mallek, S. Liu, B. B. Trinh, P. P. Shetty, G. S. Girolami and J. R. Abelson, *J. Vac. Sci. Technol., A*, 2019, **37**, 031509.
- 13 H.-U. Blaser, A. Indolese, A. Schnyder, H. Steiner and M. Studer, *J. Mol. Catal. A: Chem.*, 2001, **173**, 3–18.
- 14 U. Dingerdissen, A. Martin, D. Herein and H. J. Wernicke, *The Development of Industrial Heterogeneous Catalysis, in Handbook of Heterogeneous Catalysis*, Wiley-VCH, Weinheim, 2008, pp. 37–56.
- 15 J. A. Schaidle and L. T. Thompson, *J. Catal.*, 2015, **329**, 325–334.
- 16 L. Volpe and M. Boudart, *J. Phys. Chem.*, 1986, **90**, 4874–4877.
- 17 J. Pan, H. A. Hansen and T. Vegge, *J. Mater. Chem. A*, 2020, **8**, 24098–24107.
- 18 G. S. Ranhotra, G. W. Haddix, A. T. Bell and J. A. Reimer, *J. Catal.*, 1987, **108**, 24–39.
- 19 J.-G. Choi, M.-K. Jung, S. Choi, T.-K. Park, I. H. Kuk, J. H. Yoo, H. S. Park, H.-S. Lee, D.-H. Ahn and H. Chung, *Chem. Soc. Jpn*, 1997, **70**, 993–996.
- 20 S. T. Oyama, *J. Catal.*, 1983, **79**, 445–450.
- 21 W. Lengauer, A. Eder and R. B. King, *Encycl. Inorg. Chem. Second Ed.*, 2017, **VI**, 3315–3531.
- 22 A. Fuertes, *Mater. Horiz.*, 2015, **2**, 453–461.
- 23 S. Kim, H. J. Gwon, S. W. Paek, S. K. Kim, J. W. Choi, J. S. Kim, J. H. Choi, C. Y. Kang and S. H. Baek, *Sci. Rep.*, 2018, **8**, 2–9.
- 24 J. S. J. Hargreaves and A. R. McFarlane, *Nitride Ceramics: Combustion Synthesis, Properties and Applications*, Wiley-VCH, 2014, pp. 295–320.
- 25 P. Mishra, J. Theerthagiri and R. Panda, *Adsorpt. Sci. Technol.*, 2014, **32**, 465–474.
- 26 J. W. Huang, H. Peng and G. B. Xia, *Ironmaking Steelmaking*, 2009, **36**, 110–114.
- 27 B. Vaidhyanathan, D. K. Agrawal and R. Roy, *J. Mater. Res.*, 2000, **15**, 974–981.
- 28 B. Vaidhyanathan and K. J. Rao, *Chem. Mater.*, 1997, **9**, 1196–1200.
- 29 T. Huang, S. Mao, G. Zhou, Z. Wen, X. Huang, S. Ci and J. Chen, *Nanoscale*, 2014, **6**, 9608–9613.
- 30 Y. C. Hong, D. H. Shin and H. S. Uhm, *Mater. Chem. Phys.*, 2007, **101**, 35–40.
- 31 M. A. Roldan, V. López-Flores, M. D. Alcalá, A. Ortega and C. Real, *J. Eur. Ceram. Soc.*, 2010, **30**, 2099–2107.
- 32 O. Merdrignac-Conanec, K. El Badraoui and P. L'Haridon, *J. Solid State Chem.*, 2005, **178**, 218–223.
- 33 A. M. Glushenkov, D. Hulicova-Jurcakova, D. Llewellyn, G. Q. Lu and Y. Chen, *Chem. Mater.*, 2010, **22**, 914–921.
- 34 K. T. Jacob, R. Verma and R. M. Mallya, *J. Mater. Sci.*, 2002, **37**, 4465–4472.
- 35 D. V. Baxter, M. H. Chisholm, G. J. Gama, V. F. DiStasi, A. L. Hector and I. P. Parkin, *Chem. Mater.*, 1996, **8**, 1222–1228.



- 36 C. W. Bale, E. Bélisle, P. Chartrand, S. A. Decterov, G. Eriksson, A. E. Gheribi, K. Hack, I.-H. Jung, Y.-B. Kang, J. Melançon, A. D. Pelton, S. Petersen, C. Robelin, J. Sangster, P. Spencer and M.-A. Van Ende, *Calphad*, 2016, **54**, 35–53.
- 37 F. Tessier, *Materials*, 2018, **11**(1), 1131.
- 38 W. Lengauer and A. Eder, in *Encyclopedia of Inorganic and Bioinorganic Chemistry*, ed. Scott, R.A., Transition Metal Solid-State Chemistry, John Wiley & Sons, Ltd., Hoboken, 2015, 197–213.
- 39 P. Rodríguez, J. L. Brito, A. Albornoz, M. Labadí, C. Pfaff, S. Marrero, D. Moronta and P. Betancourt, *Catal. Commun.*, 2004, **52**, 79–82.
- 40 K. Balasubramanian, S. V. Khare and D. Gall, *Acta Mater.*, 2018, **159**, 77–88.
- 41 C. M. Ghimbeu, E. Raymundo-Piñero, P. Fioux, F. Béguin and C. Vix-Guterl, *J. Mater. Chem.*, 2011, **21**, 13268–13275.
- 42 G. H. An, D. Y. Lee and H. J. Ahn, *J. Mater. Chem. A*, 2017, **5**, 19714–19720.
- 43 H. Hui Liu, H. Ling Zhang, H. bin Xu, T. Ping Lou, Z. Tong Sui and Y. Zhang, *Ceram. Int.*, 2018, **44**, 1583–1588.
- 44 U. Zubair, S. Bianco, J. Amici, C. Francia and S. Bodoardo, *J. Power Sources*, 2020, **461**, 228144.
- 45 I. Mjejri, A. Rougier and M. Gaudon, *Inorg. Chem.*, 2017, **56**, 1734–1741.
- 46 A. Ortega, M. A. Roldan and C. Real, *Int. J. Chem. Kinet.*, 2006, **38**, 369–375.
- 47 A. I. Gusev, D. A. Davydov and A. A. Valeeva, *J. Alloys Compd.*, 2011, **509**, 1364–1372.